PROCEEDINGS OF SCIENCE

# Qudit-based quantum computing with SRF cavities at Fermilab

**Tanay Roy,**[a,*] **Taeyoon Kim,**[a,b] **Alexander Romanenko**[a] **and Anna Grassellino**[a]

[a] *Superconducting Quantum Materials and Systems Division, Fermi National Accelerator Laboratory (FNAL),*
*Batavia, IL 60510, USA*

[b] *Department of Physics and Astronomy, Northwestern University,*
*Evanston, IL 60208, USA*

*E-mail:* roytanay@fnal.gov

Superconducting radio frequency (SRF) cavities provide an excellent platform for storing quantum information as quantum $d$-level systems (qudits) due to their exceptionally long lifetimes and large accessible Hilbert spaces. A common strategy to manipulate the states is to use a nonlinear element like a transmon. There are, however, several challenges to building a 3D SRF architecture while maintaining a long cavity lifetime. We demonstrate our successful integration of transmons with single-cell Nb SRF cavities and the ability to prepare several non-classical states. Finally, we discuss our strategies to improve the coherence times, gate schemes, and extend the system for building a multi-qudit quantum processor.

*The 40th International Symposium on Lattice Field Theory (Lattice 2023)*
*July 31st - August 4th, 2023*
*Fermi National Accelerator Laboratory*

[*] Speaker





PoS(LATTICE2023)127

## 1. Introduction

Gauge theories are fundamental in the field of high-energy physics (HEP), and they play a crucial role in addressing several key problems including quantum chromodynamics, electroweak unification, Higgs mechanism and even physics beyond the standard model. Discretizing gauge theories on a spacetime lattice leads to lattice filed theories enabling powerful numerical simulations of complex physical systems that cannot be solved analytically. Consequently, tremendous advancements have been achieved in developing classical hardware and algorithms, Markov Chain Monte Carlo (MCMC) technique being one of the most popular one. Despite the great success of classical numerical methods, several problems become intractable under certain important parameter regimes due to the so-called sign problem. Recent theoretical studies have proposed that these obstacles can be circumvented by utilizing quantum algorithms [1, 2]. For example, several resource-efficient quantum algorithms for (1+1), (2+1) and (3+1) dimensional gauge theories have been developed [3–10]. However, only proof-of-principle demonstrations have been made so far for the case of (1+1) [11–15] and (2+1) [16] using currently available Noisy Intermediate-Scale Quantum (NISQ) devices [17]. Significant improvements need to be made on both quantum hardware and control schemes to realize the ambitious goal of computing (3+1) dimensional phenomena using a quantum computer.

The Superconducting Quantum Materials and Systems (SQMS) center, led by Fermilab, is dedicated to bring transformational advancements in the field of quantum computing and sensing. Its core objective is to address the decoherence challenges inherent in current quantum devices, paving the way for enhanced quantum processors and sensors. Central to this initiative is the development of three-dimensional (3D) superconducting cavity-based digital quantum computing systems within the SQMS center aimed to solve important HEP problems. These systems, utilizing 3D superconducting radio-frequency (SRF) cavities originally designed for accelerator physics, present distinct advantages over conventional 2D superconducting devices. Firstly, the fundamental mode of the 3D cavities boasts lifetimes surpassing two seconds, rendering them exceptional for storing and manipulating quantum information [18]. Secondly, efficient control and readout schemes significantly reduce cryogenic and room-temperature hardware overhead. Lastly, the inherent access to large Hilbert spaces provides the potential for direct encoding of "qudits," offering advantages in simulations compared to the conventional two-level (qubit) encoding [19].

This proceeding is organized as follows. In Sec. 2 we briefly review superconducting circuits, in particular, the circuit quantum electrodynamics (cQED) architecture for transmon qubits. In Sec. 3, we introduce the 3D SRF quantum computing system and discuss recent experimental progress in Sec. 4, followed by concluding remarks in Sec. 5.

## 2. Superconducting circuits

In the dynamic landscape of quantum computing, superconducting circuits operating at millikelvin temperatures have emerged as a leading candidate, offering a promising avenue for constructing a scalable framework. Fabricated through conventional nanolithographic techniques and controlled by microwave frequency signals, these circuits have witnessed remarkable advancements over the past 25 years including enhanced coherence times, high-fidelity measurements, and precise

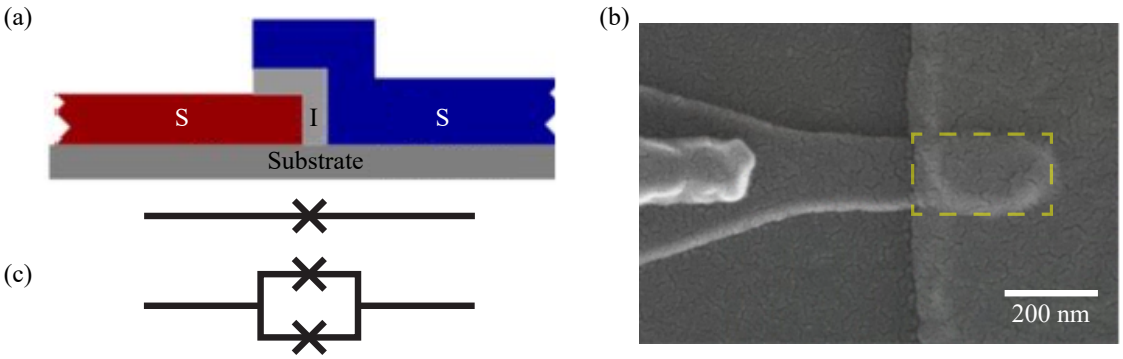


**Figure 1:** The Josephson junction. (a) A JJ is formed by a thin insulating layer sandwiched between two superconductors. It is represented by a cross in a circuit diagram. (b) A scanning electron micrograph highlighting the overlap of two metals forming the JJ. (c) A SQUID loop is formed by connecting two JJs using superconducting wires.

manipulation [20]. In the following sections we discuss the major aspects of superconducting circuits.

### 2.1 The Josephson junction

At the heart of superconducting circuits, lies a component called Josephson junction (JJ). It is composed of a thin insulating layer (typically made of some oxide) sandwiched between two superconducting material and represented with cross as illustrated in Fig. 1(a). A scanning electron micrograph of a JJ is shown in Fig. 1(b). The JJs are governed by the following Josephson relations,

$$I = I_0 \sin\delta, \tag{1a}$$

$$V = \varphi_0 \dot{\delta}, \tag{1b}$$

where, the current flowing through the junction $I$ depends on the critical current $I_0$ and the superconducting phase difference $\delta$ across the junction. The voltage $V$ across the junction is set by the time derivative of $\delta$, where $\varphi_0 = \hbar/(2e)$ is the reduced flux quantum, with $\hbar$ being the reduced Planck constant. It can be shown that the inductance $L_J$ of the JJ depends on the current flowing through it as,

$$L_J = \frac{\varphi_0}{\sqrt{I_0^2 - I^2}}, \tag{2}$$

where $L_{J0} = \varphi_0/I_0$ is the minimum inductance of the junction. As a result the JJ acts like a nonlinear lossless inductor when cooled below its superconducting transition temperature. The maximum inductance of a JJ can further be tuned by replacing a single junction by two junctions connected in a loop (see Fig. 1(c)) and threading a magnetic flux $\phi_{\text{ext}}$ through it. This structure is known as Superconducting Quantum Interference Device or SQuID loop providing a flux-dependent inductance

$$L_J(\phi_{\text{ext}}) = \frac{\varphi_0}{\sqrt{I_0^2 - I^2}} \frac{1}{\cos\phi_{\text{ext}}}. \tag{3}$$

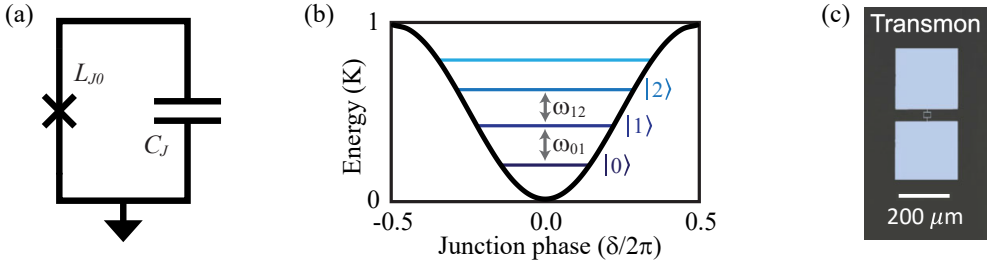


**Figure 2:** A transmon qubit. (a) A transmon is constructed by shunting a JJ using a large capacitor. (b) The cosinusoidal potential gives rise to unequally spaced energy eigenstates. The bottom two levels can thus be selectively addressed forming an effective qubit. (c) An optical image of a typical transmon qubit.

Traditionally, the JJ has been formed through Al-$Al_2O_3$-Al trilayer. However, recent studies are exploring other materials to make the JJ resilient against quasi-particles (broken Cooper pairs) or small magnetic fields [21, 22].

### 2.2 The Transmon qubit

A generic superconducting circuit takes shape through the utilization of superconducting metallic films, typically composed of materials such as Aluminum, Niobium, or Tantalum. These films are patterned on a substrate, commonly silicon or sapphire. Employing (optical and electron-beam) nanolithographic techniques, the designed patterns give rise to various electrical components, including linear inductors, linear capacitors, transmission lines, and Josephson junctions. These components are strategically interconnected in different geometries and with diverse parameters to forge resonators, which can exhibit both linear and nonlinear behaviors. As elucidated in the preceding section, the nonlinearity primarily stems from the Josephson junction.

Among the myriad superconducting circuits employed as qubits, the transmon [23] stands out as one of the most widely adopted globally due to its simple geometry, reproducible performance, good coherence times, ease of control, and precise readout. At its core, a transmon in its simplest form comprises a single Josephson junction with inductance $L_{J0}$ shunted by a large capacitor with capacitance $C_J$ as depicted in Fig. 2(a). Due to the nonlinearity introduced by the JJ, the potential energy takes on a cosinusoidal (periodic) nature, deviating from the parabolic form observed in a harmonic oscillator. This nonlinearity results in unevenly spaced energy eigenstates, as illustrated in Fig. 2(b). The lowest transition frequency, denoted as $\omega_{01}$, between the ground state and the first excited state is approximately determined by

$$\omega_{01} \simeq \frac{1}{\sqrt{L_{J0}C_J}} - E_C, \tag{4}$$

where $E_C = e^2/(2C_J)$ represents the charging energy. The second transition energy, $\omega_{12} = \omega_{01} + \eta$, differs from the first by the anharmonicity $\eta \simeq -E_C$. Typically, an anharmonicity value of $\eta \sim -250$ MHz proves adequate to selectively address the $\omega_{01}$ transition, even in the presence of multiple low-lying levels. Consequently, the ability to operate in isolation on the bottom two energy levels of the transmon circuit facilitates the creation of an effective qubit. Introducing a SQUID in place of the single junction further allows for tunability of the qubit frequency $\omega_{01}$ through the application

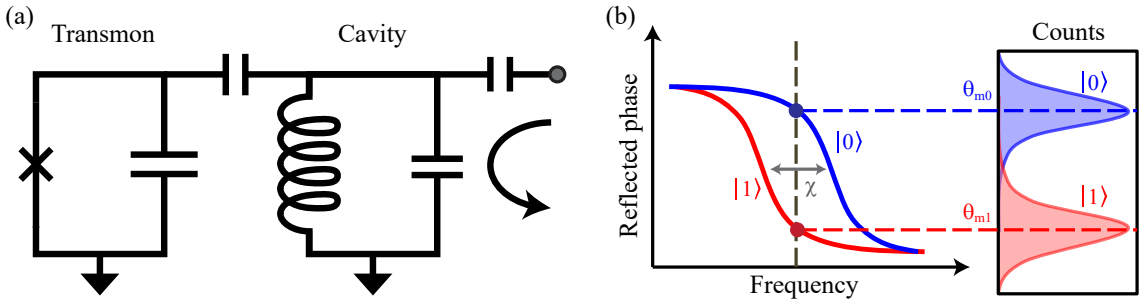


**Figure 3:** The circuit QED architecture. (a) A transmon is dispersively coupled to a linear cavity. The state of the transmon can be measured by interrogating the cavity with a microwave drive at its resonance frequency. (b) The frequency of the cavity changes by the dispersive shift $\chi$ when the qubit jumps from its ground state $|0\rangle$ to the excited state $|1\rangle$. Consequently, the cavity develops a qubit state-dependent response which leads to distinguishable signals for the two qubit states.

of an external magnetic field $\phi_{\text{ext}}$. Figure 2(c) shows an optical image of a transmon circuit with two metallic pads connected by a SQUID loop.

The device parameters for a transmon are typically selected to ensure that the qubit frequency $\omega_{01}/2\pi$ falls within the range of 3 to 6 GHz, and the anharmonicity lies between 150 and 300 MHz. This specific choice of $\omega_{01}$ introduces an additional requirement related to the operating temperature. It is essential to guarantee that the thermal energy of the device is significantly smaller than the energy associated with a photon at the transition frequency. In essence, if the physical temperature $T_{\text{tmon}}$ satisfies the condition $k_B T_{\text{tmon}} \ll \hbar\omega_{01}$, where $k_B$ is the Boltzmann constant, the qubit predominantly begins in its ground state $|0\rangle$. This necessity mandates that transmon qubits be operated at temperatures (around 10 mK) much lower than the superconducting transition temperature $T_c$.

### 2.3 The circuit QED architecture

Cavity Quantum Electrodynamics (Cavity-QED) involves examining the interaction between a single atom and the electromagnetic field of a Fabry-Perot cavity. Circuit QED (cQED) is the circuit-based realization of this concept [20, 24], where a superconducting qubit, often referred to as an artificial atom, interacts with a superconducting resonator fabricated either in a planar on-chip geometry or within a 3D waveguide cavity. The basic circuit diagram of a cQED setup is illustrated in Fig. 3(a). This system is aptly described by the Jaynes-Cummings Hamiltonian

$$H = -\frac{\hbar\omega_{01}}{2}\sigma_z + \hbar\omega_c\left(a^\dagger a + \frac{1}{2}\right) + \hbar g(a\sigma_+ + a^\dagger\sigma_-), \tag{5}$$

comprising three terms. The first term, involving the Pauli-Z operator, represents the qubit, while the second term denotes the cavity energy with a resonance frequency $\omega_c$, and the third term describes the qubit-cavity interaction under the rotating-wave approximation, wherein energy non-conserving terms are excluded. In this context, $g$ stands for the exchange coupling strength between the qubit and the cavity, $a$ ($a^\dagger$) denotes the cavity annihilation (creation) operator, and $\sigma_\pm = (\sigma_x \mp i\sigma_y)/2$ represents the qubit raising and lowering operators. The term $a^\dagger a$ is called the photon number operator whose eigenvalue is $n$ for Fock state $|n\rangle$, i.e. $a^\dagger a\,|n\rangle = n\,|n\rangle$. The non-diagonal Hamiltonian

in Eq. (5) becomes diagonalizable when the qubit-cavity detuning $|\Delta| = |\omega_{01} - \omega_c| \gg g$. In this dispersive approximation, where there is no actual photon exchange between the qubit and the cavity, the Jaynes-Cummings Hamiltonian reduces to

$$H = -\frac{\hbar\omega_{01}}{2}\sigma_z + \hbar\left(\omega_c - \frac{\chi}{2}\sigma_z\right)\left(a^\dagger a + \frac{1}{2}\right), \tag{6}$$

with $\chi \approx 2g^2/\Delta$ termed as the dispersive shift. The coefficient of $a^\dagger a$ in Eq. (6) determines the cavity's resonance frequency, which now exhibits two values separated by $\chi$ depending on the eigenvalue of $\sigma_z$ $(= \pm 1)$. Consequently, the cavity manifests two distinct responses conditioned on the state of the qubit, as illustrated in Fig 3(b). This characteristic is employed for qubit measurement, a topic elaborated in the following section.

### 2.4 Qubit measurements

The dispersive interaction described in Eq. (6) facilitates a quantum non-demolition measurement of the qubit. This is achievable because the qubit-cavity interaction term ($\propto \sigma_z a^\dagger a$) commutes with the bare qubit Hamiltonian ($\propto \sigma_z$). Consequently, the qubit's eigenstate becomes a simultaneous eigenstate of the measurement operator. When the cavity is energized, the coherent state becomes entangled with the qubit's state, and the measurement apparatus gauges the leaked coherent state either through reflection or transmission. In Fig. 3(b), the phase response of the cavity is depicted when the qubit is in its ground or excited state. If the qubit is perfectly entangled with the cavity, detecting the coherent state in one of the two possible phase values ($\theta_{m0/m1}$) results in the qubit being projected into the corresponding eigenstate. This operation is termed a strong measurement, where the qubit's wavefunction is said to collapse to either $|0\rangle$ or $|1\rangle$. However, perfect projection requires the coherent states corresponding to the qubit states to be perfectly resolved, which in practice means a well-resolved phase response (in general complex signal) of the scattered signal (see Fig. 3(b)). The resolvability depends on several factors including the dispersive shift $\chi$, cavity's linewidth, power of the probe signal, losses in the measurement chain and integration time of the output signal.

The cavity employed for qubit state measurement is referred to as the readout cavity or readout resonator, and it can be constructed in either a 2D or 3D geometry. Typical 2D structures encompass $\lambda/2$, $\lambda/4$ coplanar-waveguide or stripline configurations, or lumped-element resonators [25]. On the other hand, prevalent 3D cavities involve rectangular or coaxial geometries. Additionally, the cavity functions as a filter, positioned between the qubit and the environment, playing a pivotal role in shielding the qubit from environmental noise.

### 2.5 Decoherence

To manipulate a qubit effectively, it must be coupled to the environment to enable interaction with external signals. However, this coupling introduces undesirable noise, leading to the loss of quantum information through a process known as decoherence. Decoherence manifests in two forms: relaxation and dephasing. In the relaxation process, when a qubit is initially prepared in its excited state, it eventually loses a photon and transitions to the ground state. The characteristic time scale of this relaxation is denoted as the $T_1$ time, typically around 100 $\mu$s for typical transmon qubits in modern processors, corresponding to quality factors in the order of a few million.

Dephasing noise induces the loss of coherence in a superposition state $|\psi\rangle = c_0 |0\rangle + c_1 |1\rangle$, arising from fluctuations in qubit frequency due to various factors, including charge noise, flux noise, and shot noise. The dephasing time constant $T_\phi$ for transmon qubits is generally below 100 $\mu$s. For the effective operation of a quantum computer, it is crucial to complete all calculations within the $T_1$ and $T_\phi$ times to minimize error accumulation.

## 3. Superconducting cavities for quantum computing

Three-dimensional superconducting cavities typically exhibit significantly higher quality factors compared to their two-dimensional counterparts. As a result, numerous research groups are investigating the potential of storing and processing quantum information using 3D cavities [25–29], capitalizing on their extended lifetimes. At Fermilab, there is active exploration into the utilization of TESLA-shaped superconducting radio-frequency cavities, initially designed for accelerator physics, which currently hold the record for the highest quality factor at microwave frequencies [18].

### 3.1 Advantages of SRF cavities

Several advantages arise when using 3D SRF cavities compared to 2D transmon circuits for quantum information storage, with the primary advantage being enhanced coherence properties. While extensive efforts are dedicated to improving the $T_1$ of transmon qubits toward the millisecond range [30–32], TESLA-shaped SRF cavities have already demonstrated relaxation times exceeding 300 ms for 5 GHz resonators at dilution temperatures ($\sim 10$ mK) [18]. This three-order-of-magnitude improvement in lifetimes positions SRF cavities as significantly superior quantum memory devices. Additionally, the inherent linearity of the cavity architecture contributes to much longer $T_\phi$ times.

The second advantage arises from the large accessible Hilbert space of a single mode in SRF cavities, which operate as linear oscillators. These cavities have an infinite number of energy eigenstates, known as Fock levels (see Fig. 4(a)). The $T_1$ time corresponds to the lifetime of a coherent state or the Fock level $|1\rangle$. The lifetime of the $n$-th Fock level is given by $T_1^{(n)} = T_1^{(1)}/n$. Consequently, the Fock level $|100\rangle$ should have a lifetime longer than 3 ms, a significantly larger number compared to modern transmons. This opens avenues for using SRF cavities as qudits—$d$-dimensional quantum objects—rather than confining to just two levels for qubits. Several theoretical studies have highlighted the advantages of directly encoding HEP problems into qudits, requiring fewer operations [33–36] and potentially better noise tolerance [37, 38]. While one could argue for using transmons as qudits [39–41], there are two major issues. First, a transmon has only a few bounded energy eigenstates, and charge noise grows exponentially with Fock number, severely impacting dephasing time [23]. Consequently, practical control beyond 4 levels (Fock $|0\rangle$ through $|3\rangle$) of a transmon becomes challenging. SRF cavities on the other hand do not suffer from similar dephasing issues.

The third advantage stems from the simplicity of control and readout. Traditional 2D architectures with transmons use a linear chain or planar geometry with nearest-neighbor coupling to scale up, and the Hilbert space grows exponentially as $2^N$, where $N$ is the number of qubits. Typically, these systems need one or two input lines per qubit, one readout line for one to seven qubits, and additional input lines for tunable inter-qubit couplers. Clearly, the number of room temperature and cryogenic electrical components increases linearly with the number of qubits. In contrast, one

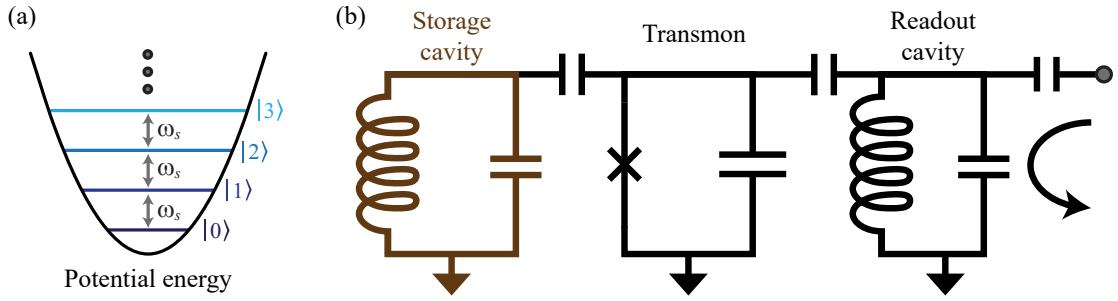


**Figure 4:** The SRF qudit architecture. (a) A linear resonator has a parabolic potential giving rise to infinitely many equally spaced energy eigenstates. (b) A transmon qubit is dispersively coupled to two linear resonators. The high-Q storage cavity holds the quantum information for a long time. The low-Q readout cavity is used to measure the state of the qubit.

$d$-dimensional mode effectively encodes $\log_2 d$ qubits, requiring just one input and output line to control that many qubits (discussed in detail later). Scaling up can be achieved by constructing multimode cavities, again without needing additional cryogenic lines or control hardware and with the benefit of obtaining $d^N$-dimensional Hilbert space.

### 3.2 Qudit control

A harmonic oscillator possesses an infinite number of evenly spaced energy eigenstates (see Fig. 4(a)). When a microwave drive is applied at the resonance frequency, it simply generates a coherent state, which is a classical state and can be expressed as

$$|\alpha\rangle = e^{-|\alpha|^2/2} \sum_{n=0}^{\infty} \frac{\alpha^n}{\sqrt{n!}} |n\rangle \,, \tag{7}$$

where $|\alpha|^2$ represents the average number photons in the coherent state $|\alpha\rangle$. This kind of classical drive that creates one coherent state from another (including the ground state $|0\rangle$) is called the displacement operation. Thus, controlling individual Fock levels directly is not possible without the assistance of some nonlinear component. We employ the Jaynes-Cummings Hamiltonian for executing quantum operations (also known as gates) and for preparing non-classical states inside the cavity. A simplified circuit diagram is depicted in Fig. 4(b), illustrating a high-Q storage cavity (with resonance frequency $\omega_s$) coupled with a transmon. This coupling enables the execution of quantum gates on the storage, holding quantum information in its 3D electromagnetic field. The transmon is also linked to a resonator for the readout of both the transmon and the storage. Focusing on the storage and transmon (with $\omega_{01} = \omega_q$) interaction, similar to Eq. (6), the Hamiltonian can be written as

$$H_s = \hbar\omega_s \left( b^\dagger b + \frac{1}{2} \right) - \hbar(\omega_q + \chi_s b^\dagger b) \frac{\sigma_z}{2}, \tag{8}$$

where, $b$ ($b^\dagger$) is the annihilation (creation) operator for the storage mode and $\chi_s$ is the dispersive shift between the transmon and the storage. Henceforth, we will use $|g\rangle$ and $|e\rangle$ to represent the ground and first excited states of the transmon respectively and treat it as a qubit.

Unlike Eq. (6), the dispersive interaction term $\hbar\chi_s b^\dagger b\sigma_z/2$ is combined with the qubit term in Eq. (8). Therefore, the second term implies that the qubit's frequency depends on the photon number of the storage mode. For instance, the qubit frequency $\omega_q^{(0)} = \omega_q$ when the storage is in its ground state $|0\rangle$ changes to $\omega_q^{(1)} = \omega_q + \chi_s$ when the storage is excited to $|1\rangle$. In general, if there are $n$ photons in the storage, the effective qubit frequency is given by

$$\omega_q^{(n)} = \omega_q + n\chi_s. \tag{9}$$

If the qubit's linewidth is much smaller than $\chi_s$, these frequencies become well-resolved and can be employed to execute non-classical operations on the storage mode's state, a process known as Selective Number-dependent Arbitrary Phase (SNAP) gate [42, 43].

To understand the working principle of a SNAP gate, consider a superposition state $\sum_{k=0}^{d} c_k |k\rangle$ in the storage along with the qubit being in its ground state $|g\rangle$. The joint state of the storage and qubit can be expressed as

$$|\psi\rangle = \sum_{k=0}^{d} c_k |k\rangle \otimes |g\rangle , \tag{10}$$

with $\sum_{k=0}^{d} |c_k|^2 = 1$. Now, if we apply a full $2\pi$ rotation on the qubit conditioned on having $n$ photons in the storage by applying a microwave drive at $\omega_q + n\chi_S$, the basis component $|n\rangle$ obtains a phase kick-back resulting in

$$|\psi'\rangle = \left(\sum_{k\neq n} c_k |k\rangle - c_n |n\rangle\right) \otimes |g\rangle . \tag{11}$$

In general, by splitting the $2\pi$ rotation into two $\pi$ pulses and adjusting the relative phase of the second $\pi$ pulse, arbitrary phase can be imparted on any basis component. The final state after a typical SNAP operation is given by

$$\left|\psi_f\right\rangle = \left(\sum_{k=0}^{d} c_k e^{i\theta_k} |k\rangle\right) \otimes |g\rangle . \tag{12}$$

It is noteworthy that the final state is a product state, with the qubit returning to its initial state $|g\rangle$, thereby completing the gate operation. A general SNAP gate $\hat{S}$ can thus be expressed as

$$\hat{S}(\vec{\theta}) = \sum_{k=0}^{d} e^{i\theta_k} |k\rangle \langle k| , \ \theta_k \in [0, 2\pi], \tag{13}$$

with $\vec{\theta} = \{\theta_0, \theta_1, \cdots, \theta_d\}$. The SNAP gates, in conjunction with the displacement gate $\hat{D}(\alpha) = e^{\alpha b^\dagger - \alpha^* b}$, constitute a universal gate set. Consequently, any arbitrary unitary operation can be achieved through the alternating application of SNAP and displacement gates. It is important to note that the driving strength for a SNAP gate should be much smaller than $\chi_s$ to make it conditional. A general rule of thumb is to use a pulse length of $\pi/(10\chi_s)$ which theoretically reduces the coherent error due to off-resonant driving to 1%. On the contrary, the displacement should be much faster and broadband to make it independent of the state of the qubit. An alternative universal gate set is formed by echoed-conditional gate and single qubit rotations, which are tailored for the systems where the dispersvie shift $\chi_s$ is much smaller than the linewidth of the qubit [44].

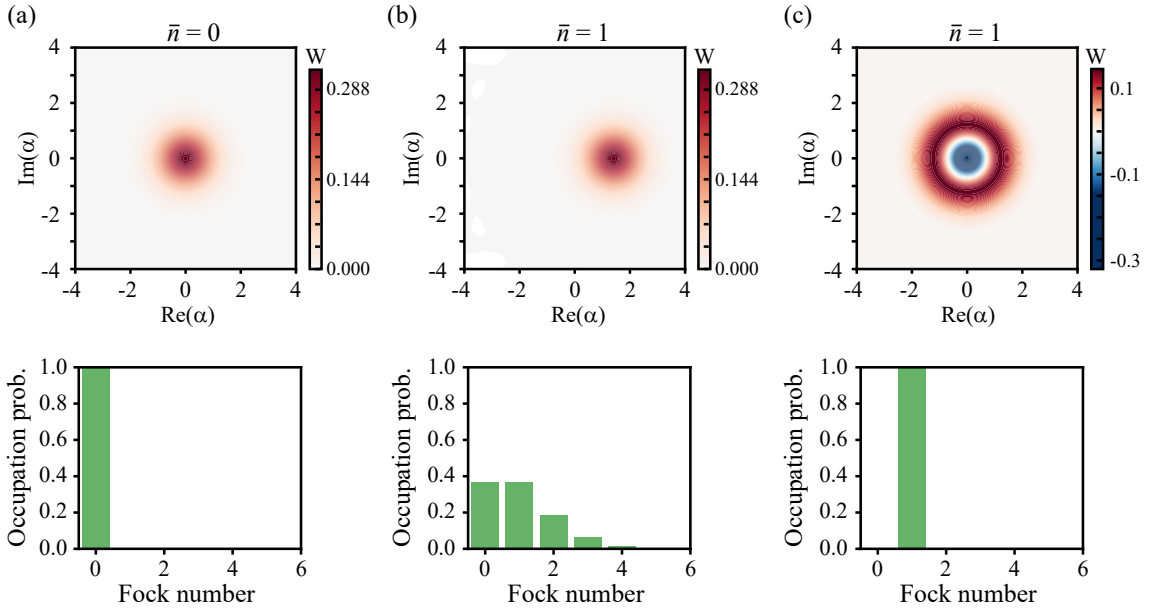


**Figure 5:** Ideal Wigner tomography (top panel) and corresponding Fock state occupation probability (bottom panel) for (a) the ground state $|0\rangle$, (b) a coherent state ($\alpha = 1$) with an average photon number $\bar{n} = 1$, and (c) the Fock state $|1\rangle$. Note that the populations are distributed across multiple Fock states for the coherent state.

### 3.3 Qudit measurement

To determine the population of the basis components, a strategy akin to the SNAP gate operation can be employed. Instead of applying a $2\pi$ rotation, a $\pi$ pulse on the qubit conditioned on the presence of $n$ photons in the storage can be applied. The resultant state following this operation is given by

$$|\psi'\rangle = \sum_{k \neq n} c_k |k\rangle \otimes |g\rangle + c_n |n\rangle \otimes |e\rangle , \tag{14}$$

forming an entangled state between the storage and the qubit. Subsequently, if the qubit is measured using the readout resonator (refer to Fig. 4(b)), it collapses to $|e\rangle$ with a probability $|c_n|^2$, while concurrently, the cavity is projected to $|n\rangle$. By repeating the measurements a large number of times after applying the conditional $\pi$ pulses on the same initial state, the relative weights can also be obtained.

A complete characterization of the state is achievable through Wigner tomography [45], a technique that gauges the parity of the state following displacements with varying amplitudes and phases. The parity operator, denoted as $\hat{\Pi}$, is defined by

$$\hat{\Pi} = e^{i\pi b^\dagger b}, \tag{15}$$

where it yields an eigenvalue of 1 (-1) when the photon count in the storage is even (odd). Implementing the parity operator involves a Ramsey-type experiment on the qubit. In this procedure, a $\pi/2$ pulse is applied to the qubit, initializing it along the equator of the Bloch sphere. Following a wait period of $\pi/\chi_s$, another $\pi/2$ pulse with an opposite phase is applied. If the storage has an even (odd) number of photons, the qubit ends up in the ground (excited) state, which is determined

using the readout resonator. Ideal Wigner tomography for select cavity states is illustrated in Fig. 5, where a negative value of the Wigner function in the tomography signifies a non-classical state.

## 4. Experimental results

As a first step towards building a universal qudit-based quantum computer we successfully integrated a 3D transmon into a TESLA shaped SRF cavity and performed basic characterizations [25].

### 4.1 The system

The quantum information is stored in the fundamental mode ($TM_{01}$) of a TESLA-shaped 3D superconducting cavity, as illustrated in Fig. 6(a) [25, 46]. This SRF cavity comprises an elliptical resonator flanked by two cylindrical sections known as beampipes. Reflection or transmission measurements can be conducted by introducing antennas through the beampipes. The ancilla transmon is strategically positioned from one side, nearly reaching the center of the cavity to optimize electromagnetic interaction. Typically, we employ 3 or 5 GHz TESLA cavities constructed from Niobium, featuring elliptical sections typically a few centimeters in diameter. The transmon (see Fig. 6(b)) is fabricated on a silicon or sapphire substrate, utilizing various superconducting materials such as Aluminum, Niobium, or Tantalum to create the capacitor pads, while the Josephson junction is commonly made from Aluminum. The transmon's frequency ranges from 4 to 6 GHz. For the transmon readout, a higher harmonic ($TM_{11}$) of the cavity is employed.

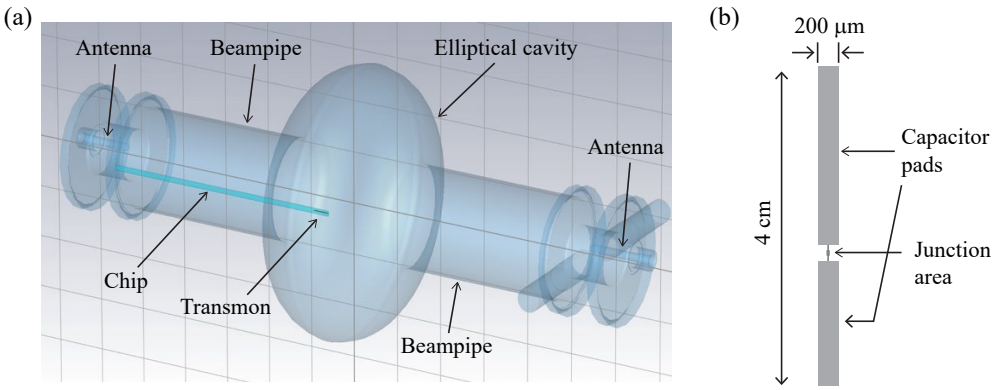


**Figure 6:** The transmon-cavity system. (a) The SRF cavity is made using Niobium. A transmon qubit is inserted through the beampipe so that it can strongly interact with the high-Q $TM_{01}$ mode. The antennas are used to deliver and collect RF signals. The readout of the transmon is performed using the $TM_{11}$ mode. (b) Typical geometry of the transmon (not to scale) consisting of two capacitor pads and a Josephson junction. The transmon is fabricated on a silicon or sapphire substrate.

### 4.2 Measurement setup

The cryogenic wiring configuration is delineated in Fig. 7. In a modern commercial dilution refrigerator, there are typically five stages, each operating at different temperatures. The innermost stage, often referred to as the base plate or mixing chamber plate, achieves the lowest temperature at around 10 mK. Attenuators on the input lines play a dual role by reducing blackbody radiation

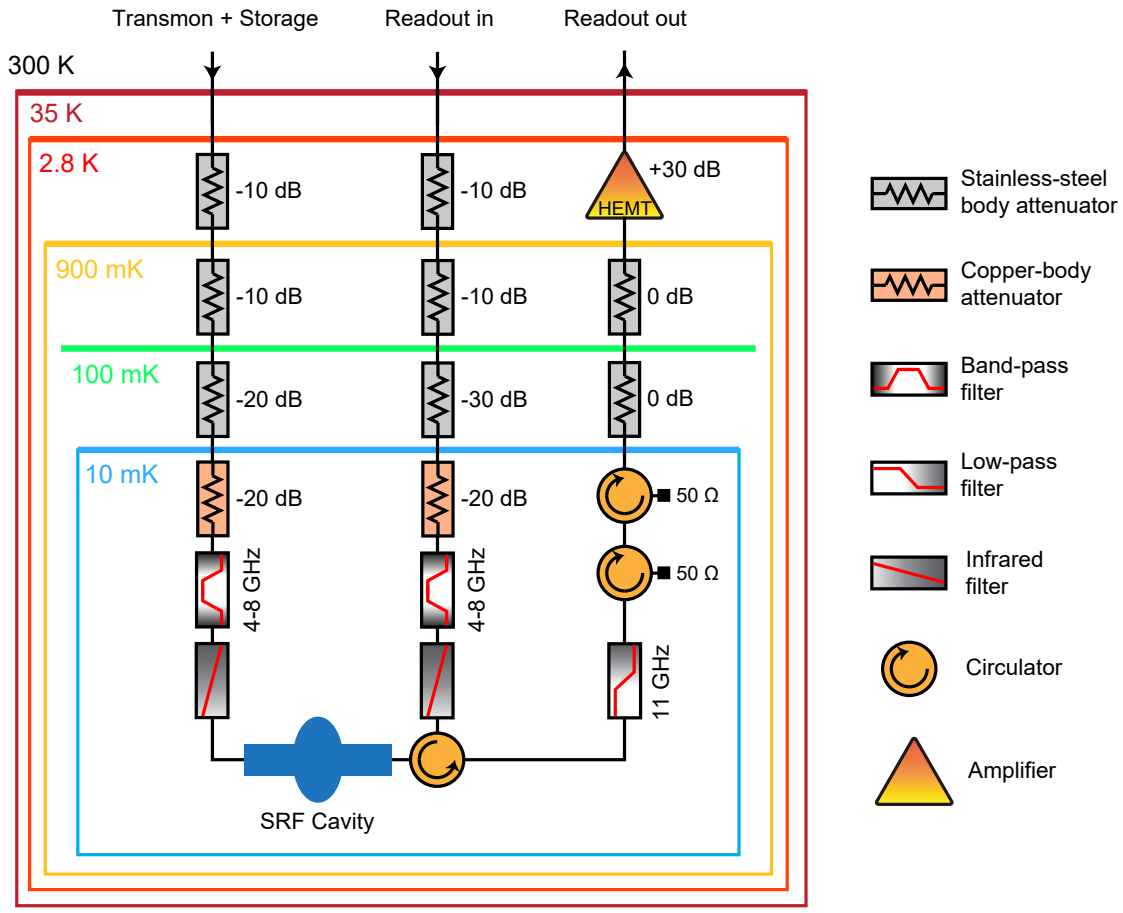


**Figure 7:** Cryogenic wiring of the setup. The pulses for the transmon qubit and storage are sent through a single RF line. Readout of the qubit is performed in reflection. The boxes represent thermal shields at specified temperatures.

originating from room temperature electronics outside the fridge and aiding in thermalizing the input lines to their respective fridge stages. Copper-body attenuators, situated closer to the device under test, exhibit superior thermal conductivity compared to their stainless-steel counterparts. Band-pass filters serve to block extraneous signals outside the frequency zone of interest, while low-pass filters reflect signals at frequencies exceeding the cut-off value. Infrared filters are strategically placed to obstruct high-energy radiation that could potentially break Cooper pairs.

A single input line is designated for sending pulses to the transmon and storage, while a separate RF line conveys readout pulses for measuring the transmon's state. The reflected signal at the readout frequency is directed toward the output line through a circulator. Two isolators, which are essentially circulators with one port terminated by a 50 Ω resistor, are introduced on the output line to shield the device from incoming radiation along the output line. Before exiting the fridge, the output signal undergoes amplification via a cryogenic high electron mobility transistor (HEMT). Typically, one or two additional room-temperature amplifiers are employed on the output line before data digitization. Microwave pulses are typically generated using an arbitrary waveform

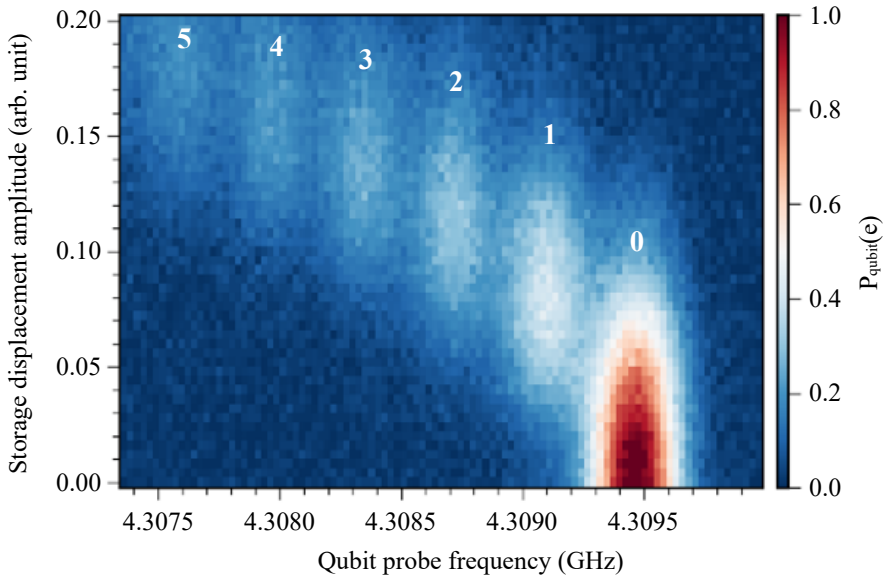


**Figure 8:** Qubit spectroscopy as a function of varying driving strengths on the storage. The on-resonance drives create coherent states with average photon numbers proportional to the square of the drive amplitude. The blobs corresponding to different Fock distribution are separated by qubit-storage dispersive shift $\chi_s/2\pi$.

generator (AWG), and the acquired signal is recorded in a computer for subsequent analysis.

### 4.3 Photon-number counting

The successful integration of a transmon with the SRF cavity is demonstrated by the observation of a photon-number-dependent qubit frequency, as described in Eq. (9). This characteristic is unveiled through qubit spectroscopy, where the storage is driven with varying strengths. In Fig. 8, the x-axis represents the probe frequency utilized for the qubit's $\pi$ pulse after applying a displacement to the storage with increasing driving amplitudes.

When no drive is applied (amplitude = 0), the storage, having zero photons, results in qubit excitation around $\omega_q$ (depicted by the red blob in Fig. 8). As a displacement is applied to the storage, coherent states with different average photon numbers are generated, with distinct photon number distributions given by Eq. (7). Consequently, the qubit responds to multiple frequencies separated by the storage-qubit dispersive shift $\chi_s$, manifesting as multiple blobs in Fig. 8.

### 4.4 Fock state preparation

An essential aspect of utilizing a cavity as a qudit involves demonstrating the preparation of Fock states. The process involves a sequence comprising alternate displacement and SNAP gates. For instance, starting from the ground state $|0\rangle$ in the storage, Fock state $|1\rangle$ can be prepared by applying (a) $\hat{D}_0(\alpha = 1.143)$, (b) $S_\pi(0)$, and (c) $\hat{D}_1(\alpha = -0.520)$. Here, $S_\theta(k)$ indicates the application of a SNAP gate with phase $\theta$ on Fock level $|k\rangle$. In Fig. 9(a), the Wigner tomography of $|1\rangle$ prepared using this sequence is depicted. The lifetime of this state was determined by measuring the average population of $|1\rangle$ after varying waiting periods, as presented in Fig. 9(b), showing a $T_1$ of about 3.1 ms.

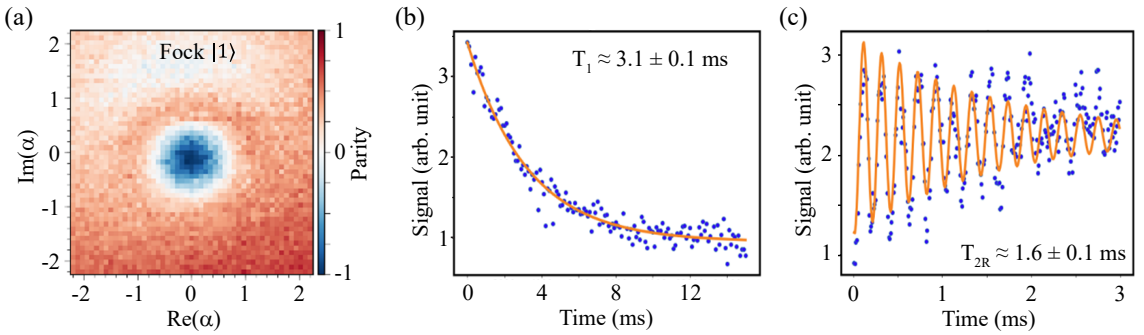


**Figure 9:** Characterization of Fock state $|1\rangle$. (a) Wigner tomography showing parity along orthogonal displacement directions. A single circular ring with 0 parity is the signature of $|1\rangle$. Data corresponding to (b) a relaxation experiment and (c) a Ramsey experiment for characterizing $T_1$ and $T_\phi$.

To measure $T_\phi$, a Ramsey-type experiment was conducted where the initial state $(|0\rangle+|1\rangle)/\sqrt{2}$ is prepared with the sequence $\hat{D}_1(\alpha = 0.243)S_\pi(0)\hat{D}_0(\alpha = -0.561)$. The resulting oscillation, shown in Fig. 9(c), exhibits a decay constant $T_{2R}$ of 1.6 ms, corresponding to a pure dephasing time $T_\phi$ of 2.1 ms. These coherence numbers significantly surpass those of a typical transmon device.

Similarly, a Fock state $|n\rangle$ can be realized (with sufficeintly low infidelity) by applying $n$ SNAP pulses and $(n+1)$ displacement pulses. Figure 10 illustrates qubit spectroscopy after various Fock states are prepared, revealing peaks at difference frequencies $n\chi_s$ from $\omega_q$. The peak heights serve as an indicator of the occupation of a specific Fock level.

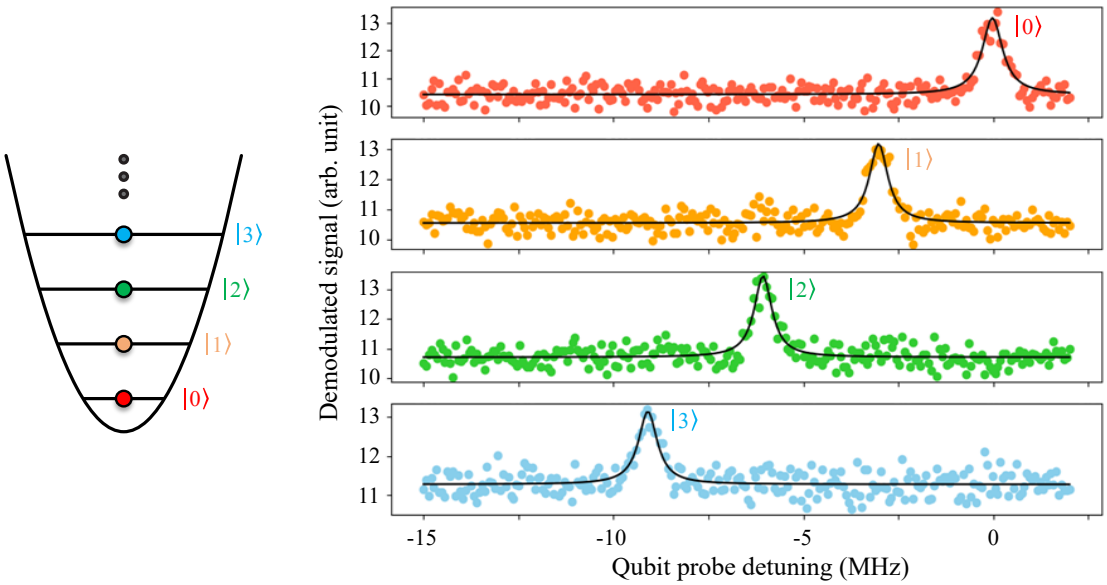


**Figure 10:** Multiple Fock states preparation. Qubit spectroscopies after preparation of Fock states $|0\rangle$ to $|3\rangle$ show the relevant peaks at detunings which are multiple of the storage-qubit dispersive shift $\chi_s/2\pi$.

## 5. Conclusion and outlook

In conclusion, the utilization of 3D SRF cavities presents a promising avenue for advancing quantum computing beyond conventional 2D superconducting circuits. The distinct advantages, including access to a large Hilbert space, extended coherence times, and a simplified control scheme, position this architecture as a compelling alternative. Besides accessing higher Fock states, the ongoing development of multi-mode cavities [47], where a common transmon controls all modes, sets the stage for the implementation of two-qudit gate schemes, particularly relevant for addressing challenges in high-energy physics.

Looking forward, immediate enhancements involve the extension of this system to incorporate multi-mode cavities, paving the way for more sophisticated algorithms targeting specific high-energy physics problems. Further scalability is envisaged through a modular architecture featuring a multi-mode storage unit and a manipulator module. The high-Q cavities in the storage unit, designed for prolonged quantum information storage akin to quantum random access memory, coupled with quantum operations in the manipulator module, present a viable path for scaling up quantum computing capabilities. The integration of a coupler element facilitates seamless quantum state transfer between the storage and manipulator modules, opening avenues for continued exploration and innovation in quantum computing.

## Acknowledgments

We thank Hank Lamm for useful discussions. This work is supported by the U.S. Department of Energy, Office of Science, National Quantum Information Science Research Centers, Superconducting Quantum Materials and Systems Center (SQMS) under contract number DE-AC02-07CH11359.

## References

[1] L. Funcke, T. Hartung, K. Jansen and S. Kühn, *Review on Quantum Computing for Lattice Field Theory*, *PoS* **LATTICE2022** (2023) 228.

[2] C. W. Bauer, Z. Davoudi, A. B. Balantekin, T. Bhattacharya, M. Carena, W. A. de Jong et al., *Quantum simulation for high-energy physics*, *PRX Quantum* **4** (2023) 027001.

[3] M. C. Bañuls, K. Cichy, J. I. Cirac, K. Jansen and S. Kühn, *Efficient basis formulation for (1 + 1)-dimensional su(2) lattice gauge theory: Spectral calculations with matrix product states*, *Phys. Rev. X* **7** (2017) 041046.

[4] A. Celi, B. Vermersch, O. Viyuela, H. Pichler, M. D. Lukin and P. Zoller, *Emerging two-dimensional gauge theories in rydberg configurable arrays*, *Phys. Rev. X* **10** (2020) 021057.

[5] D. B. Kaplan and J. R. Stryker, *Gauss's law, duality, and the hamiltonian formulation of u(1) lattice gauge theory*, *Phys. Rev. D* **102** (2020) 094515.

[6] J. F. Haase, L. Dellantonio, A. Celi, D. Paulson, A. Kan, K. Jansen et al., *A resource efficient approach for quantum and classical simulations of gauge theories in particle physics*, *Quantum* **5** (2021) 393.

[7] D. Paulson, L. Dellantonio, J. F. Haase, A. Celi, A. Kan, A. Jena et al., *Simulating 2d effects in lattice gauge theories on a quantum computer*, *PRX Quantum* **2** (2021) 030334.

[8] T. Armon, S. Ashkenazi, G. García-Moreno, A. González-Tudela and E. Zohar, *Photon-mediated stroboscopic quantum simulation of a $F_2$ lattice gauge theory*, *Phys. Rev. Lett.* **127** (2021) 250501.

[9] M. Carena, H. Lamm, Y.-Y. Li and W. Liu, *Improved Hamiltonians for Quantum Simulations of Gauge Theories*, *Phys. Rev. Lett.* **129** (2022) 051601 [2203.02823].

[10] C. W. Bauer and D. M. Grabowska, *Efficient representation for simulating u(1) gauge theories on digital quantum computers at all values of the coupling*, *Phys. Rev. D* **107** (2023) L031503.

[11] J. Liu and Y. Xin, *Quantum simulation of quantum field theories as quantum chemistry*, *Journal of High Energy Physics* **2020** (2020) 1.

[12] W. Qian, R. Basili, S. Pal, G. Luecke and J. P. Vary, *Solving hadron structures using the basis light-front quantization approach on quantum computers*, *Phys. Rev. Res.* **4** (2022) 043193.

[13] C. Charles, E. J. Gustafson, E. Hardt, F. Herren, N. Hogan, H. Lamm et al., *Simulating $\mathbb{Z}_2$ lattice gauge theory on a quantum computer*, *arXiv preprint arXiv:2305.02361* (2023) [2305.02361].

[14] G. M. Vinod and A. Shaji, *Simulating quantum field theories on gate-based quantum computers*, *arXiv preprint arXiv:2401.04496* (2024) [2401.04496].

[15] R. C. Farrell, M. Illa, A. N. Ciavarella and M. J. Savage, *Quantum Simulations of Hadron Dynamics in the Schwinger Model using 112 Qubits*, *arXiv preprint arXiv:2401.08044* (2024) [2401.08044].

[16] A. Yamamoto, *Real-time simulation of (2+1)-dimensional lattice gauge theory on qubits*, *Progress of Theoretical and Experimental Physics* **2021** (2020) 013B06 [2008.11395].

[17] J. Preskill, *Quantum Computing in the NISQ era and beyond*, *Quantum* **2** (2018) 79.

[18] A. Romanenko, R. Pilipenko, S. Zorzetti, D. Frolov, M. Awida, S. Belomestnykh et al., *Three-Dimensional Superconducting Resonators at T<20 mK with Photon Lifetimes up to $\tau$=2 s*, *Phys. Rev. Appl.* **13** (2020) 1.

[19] Y. Wang, Z. Hu, B. C. Sanders and S. Kais, *Qudits and High-Dimensional Quantum Computing*, *Front. Phys.* **8** (2020) 1.

[20] A. Blais, A. L. Grimsmo, S. M. Girvin and A. Wallraff, *Circuit quantum electrodynamics*, *Rev. Mod. Phys.* **93** (2021) 025005.

[21] M. Xu, R. Cheng, Y. Wu, G. Liu and H. X. Tang, *Magnetic field-resilient quantum-limited parametric amplifier*, *PRX Quantum* **4** (2023) 010322.

[22] J. Kroll, W. Uilhoorn, K. van der Enden, D. de Jong, K. Watanabe, T. Taniguchi et al., *Magnetic field compatible circuit quantum electrodynamics with graphene josephson junctions*, *Nature communications* **9** (2018) 4615.

[23] J. Koch, T. M. Yu, J. Gambetta, A. A. Houck, D. I. Schuster, J. Majer et al., *Charge-insensitive qubit design derived from the Cooper pair box*, *Physical Review A* **76** (2007) 042319.

[24] D. I. Schuster, *Circuit quantum electrodynamics*. Yale University, 2007.

[25] T. Roy, *Towards multi-qudit quantum processor using superconducting RF cavities*, tech. rep., Fermi National Accelerator Laboratory (FNAL), Batavia, IL (United States), 2023.

[26] A. Blais, S. M. Girvin and W. D. Oliver, *Quantum information processing and quantum optics with circuit quantum electrodynamics*, *Nature Physics* **16** (2020) 247.

[27] B. Vlastakis, G. Kirchmair, Z. Leghtas, S. E. Nigg, L. Frunzio, S. M. Girvin et al., *Deterministically encoding quantum information using 100-photon schrödinger cat states*, *Science* **342** (2013) 607.

[28] O. Milul, B. Guttel, U. Goldblatt, S. Hazanov, L. M. Joshi, D. Chausovsky et al., *Superconducting cavity qubit with tens of milliseconds single-photon coherence time*, *PRX Quantum* **4** (2023) 030336.

[29] S. Chakram, A. E. Oriani, R. K. Naik, A. V. Dixit, K. He, A. Agrawal et al., *Seamless high-q microwave cavities for multimode circuit quantum electrodynamics*, *Phys. Rev. Lett.* **127** (2021) 107701.

[30] C. Wang, X. Li, H. Xu, Z. Li, J. Wang, Z. Yang et al., *Towards practical quantum computers: transmon qubit with a lifetime approaching 0.5 milliseconds*, *npj Quantum Information* **8** (2022) 1.

[31] A. P. Place, L. V. Rodgers, P. Mundada, B. M. Smitham, M. Fitzpatrick, Z. Leng et al., *New material platform for superconducting transmon qubits with coherence times exceeding 0.3 milliseconds*, *Nature communications* **12** (2021) 1.

[32] M. Bal, A. A. Murthy, S. Zhu, F. Crisa, X. You, Z. Huang et al., *Systematic improvements in transmon qubit coherence enabled by niobium surface encapsulation*, *arXiv preprint arXiv:2304.13257* (2023) [2304.13257].

[33] E. J. Gustafson, *Prospects for simulating a qudit-based model of* (1 + 1)D *scalar qed*, *Phys. Rev. D* **103** (2021) 114505.

[34] E. J. Gustafson, H. Lamm, F. Lovelace and D. Musk, *Primitive quantum gates for an su*(2) *discrete subgroup: Binary tetrahedral*, *Phys. Rev. D* **106** (2022) 114501.

[35] T. V. Zache, D. González-Cuadra and P. Zoller, *Fermion-qudit quantum processors for simulating lattice gauge theories with matter*, *Quantum* **7** (2023) 1140.

[36] M. Meth, J. F. Haase, J. Zhang, C. Edmunds, L. Postler, A. Steiner et al., *Simulating 2d lattice gauge theories on a qudit quantum computer*, *arXiv preprint arXiv:2310.12110* (2023) [2310.12110].

[37] E. Gustafson, *Noise Improvements in Quantum Simulations of sQED using Qutrits*, *arXiv preprint arXiv:2201.04546* (2022) [2201.04546].

[38] E. J. Gustafson and H. Lamm, *Robustness of Gauge Digitization to Quantum Noise*, *arXiv preprint arXiv:2301.10207* (2023) [2301.10207].

[39] T. Roy, Z. Li, E. Kapit and D. Schuster, *Two-qutrit quantum algorithms on a programmable superconducting processor*, *Phys. Rev. Appl.* **19** (2023) 064024.

[40] L. M. Seifert, Z. Li, T. Roy, D. I. Schuster, F. T. Chong and J. M. Baker, *Exploring ququart computation on a transmon using optimal control*, *Phys. Rev. A* **108** (2023) 062609.

[41] S. Cao, M. Bakr, G. Campanaro, S. D. Fasciati, J. Wills, D. Lall et al., *Emulating two qubits with a four-level transmon qudit for variational quantum algorithms*, *arXiv preprint arXiv:2303.04796* (2023) [2303.04796].

[42] R. W. Heeres, B. Vlastakis, E. Holland, S. Krastanov, V. V. Albert, L. Frunzio et al., *Cavity state manipulation using photon-number selective phase gates*, *Phys. Rev. Lett.* **115** (2015) 137002.

[43] S. Krastanov, V. V. Albert, C. Shen, C.-L. Zou, R. W. Heeres, B. Vlastakis et al., *Universal control of an oscillator with dispersive coupling to a qubit*, *Phys. Rev. A* **92** (2015) 040303.

[44] A. Eickbusch, V. Sivak, A. Z. Ding, S. S. Elder, S. R. Jha, J. Venkatraman et al., *Fast universal control of an oscillator with weak dispersive coupling to a qubit*, *Nature Physics* **18** (2022) 1464.

[45] K. E. Cahill and R. J. Glauber, *Density operators and quasiprobability distributions*, *Phys. Rev.* **177** (1969) 1882.

[46] D. van Zanten, T. Kim, T. Roy, S. Zorzetti, M. J Reagor, M. Bal et al., *Progress on 3D qudit architecture with high-coherence SRF cavities*, *Bull. Am. Phys. Soc.* (2023) .

[47] A. Reineri, S. Zorzetti, T. Roy and X. You, *Exploration of superconducting multi-mode cavity architectures for quantum computing*, in *2023 IEEE International Conference on Quantum Computing and Engineering (QCE)*, vol. 01, pp. 1342–1348, 2023, DOI.